Hybrid Single Lap Joints between 3D Printed Titanium Lattices and CFRP Composites: Experimental and Numerical Insights

Andrea Corrado [1,*] , Raffaele De Biasi [1] , Daniele Rigotti [1] , Fabrizio Stecca [2] , Alessandro Pegoretti [1] and Matteo Benedetti [1,*]

[1] Department of Industrial Engineering, University of Trento, 38123 Trento, Italy; daniele.rigotti-1@unitn.it (D.R.); alessandro.pegoretti@unitn.it (A.P.)
[2] Novation Tech S.P.A., 31044 Montebelluna, Italy; fabrizio.stecca@novationtech.com
[*] Correspondence:andrea.corrado@unitn.it (A.C.); matteo.benedetti@unitn.it (M.B.)

Abstract: In the contemporary emphasis on weight reduction, the utilization of advanced materials like Carbon Fiber Reinforced Polymers (CFRPs) and cutting-edge technologies such as 3D printing of metal is increasingly crucial. This study delves into the junction of CFRP and titanium, aiming to conduct Single Lap shear tests on specimens featuring a co-lamination of long fiber composite onto a metal lattice structure. Different specimens with different dimensions of the Simple Cubic (SC) unit cell were subjected to testing. A microscope investigation facilitated an exploration of junction failure and epoxy resin infiltration into the lattice substrate. Employing an efficient 2D Finite Element Model, the homogenization process yielded theoretical models underestimating the Young Modulus by approximately 10% compared to real specimens. Despite the challenges in bonding titanium and CFRP, the novel junction exhibited a shear stress of 17.25 MPa, which is nearly equivalent to those of a co-lamination between sandblasted steel and CFRP, that is 17.15 MPa.

1. Introduction

In recent years, a discernible shift within engineering emphasizes the imperative of weight reduction to mitigate the environmental impact associated with human activities. This trend is particularly pronounced in the automotive and aerospace industries, where weight reduction directly correlates with improved fuel efficiency. As documented in [1], a 20% reduction in the weight of a Boeing 787 aircraft leads to a noteworthy 10% decrease in fuel consumption. The pursuit of enhanced performance propels researchers and industries to explore innovative technologies and materials. As delineated by the Ashby diagram [2], composite materials, specifically carbon fiber, are emerging as prominent solutions to lightweight challenges due to their low density, high Young Modulus, and superior ultimate tensile strength. However, a critical challenge arises in effectively integrating these elements with other solid components in complex structures. The prevalent approach involves joining carbon fiber composites using rivets/bolts or adhesive bonding [3]. To avoid failure in safety-critical components, larger inserts or multiple rivets/bolts are often employed to increase the overlap area. Unfortunately, this solution escalates the overall component weight, diminishing its performance. Classical joining techniques can introduce drawbacks. For instance, rivets must be mounted on pre-drilled components, leading to high stress concentrations around geometric discontinuities, potential damage to carbon fibers and an overall reduction in stiffness [4]. The use of glue presents challenges as well, with the possibility of degradation over time, particularly under elevated temperatures [5,6]. To address these issues, various authors propose innovative junction techniques to eliminate the need for external elements (e.g., glue, bolts, rivets) while ensuring a robust bond between metal components and composite parts. Examples include studying the influence

of superficial roughness [7] and cleaning [8] on the performance of a single lap junction, as well as advanced techniques such as Silica coatings [9], CNT application on titanium components [10] and RPC coatings [11].

Preliminary works highlight the potential of co-laminating CFRP and metal components, where mechanical bonding is directly provided by the resin without the need for additional elements. Some studies demonstrate the possibility of improving adhesion through specific patterns on the metal surface [12–14], which can also enhance the local stiffness of inserts placed in the middle of the lamination process [15,16]. This study aims to enhance the design of "Hybrid Junctions" connecting a carbon fiber component to an improved version of a metal component using specific additively manufactured shapes and patterns on the contact surface. Additive Manufacturing (AM) techniques prove beneficial, enabling the fabrication of complex shapes unattainable with classical production processes [17]. The development of AM facilitates the production of intricate lattice structures [18], known for their extreme tunability in mechanical properties, lightweight capabilities [19], high specific strength [20,21], and effective energy absorption [22].

In future research works, Hybrid Junctions can be applied to enhance the existing technique of Fiber Metal Laminates (FML). FML are composite structures composed of alternating thin metal sheets with CFRP plies [23,24]. The bonding between these materials can be improved by employing a 3D printed metal lattice structure instead of traditional thin metal sheets.

The authors undertake an exploratory study on the influence of lattice structure substrates in the production of hybrid joints. Mechanical properties are enhanced through infilled epoxy resin within the Pre-Preg CFRP, aiming to distribute loads more efficiently and prevent the buckling of unit cell struts [25,26]. Various cell dimensions and porosity levels are tested and then, compared with Finite Element (FE) simulations, providing insights into the elastic behavior of Hybrid Junctions. An efficient simulation framework based on the homogenization technique [27] is developed to optimize computational time and resources during the design phase of the components.

2. Materials and Methods

2.1. Specimen Design and Manufacturing

In order to assess the impact of lattice structures in Hybrid Junctions, shear lap specimens were devised, manufactured, and subjected to testing. The Hybrid Junctions consist of a carbon fiber composite with long fibers and a metal substrate crafted from Ti6Al4V through the Laser-Powder Bed Fusion (LPBF) Additive Manufacturing technique. To appraise the mechanical characteristics of these novel junctions, the specimens adhere to the guidelines outlined in ASTM D5868 [28]. This standardized protocol is essential for examining the bonding properties between Fiber Reinforced Plastic (FRP) and metals under shear loads, aiming to ascertain the shear strength of adhesives within the overlapping region of the junction itself.

The fabrication process of Hybrid Junctions holds paramount significance, and it unfolded through the following steps:

- Design and manufacture of a dedicated steel jig tailored to accommodate 3D printed metal components within specified slots. These slots are configured to match the thickness of the metal substrate, establishing a level surface conducive to CFRP lamination.
- Preparatory treatment of the jig to streamline the extraction of laminated parts: application of a spray sealer in three successive layers with a 10-min interval between each application. Subsequently, a liquid mold release spray is applied three times with an intermediate rest of 10 min.
- Placement of AM metal substrates into the designated slots, positioning the lattice surface toward the resin.
- Application of a layer of IMP380F only above the lattice structure on the overlap area. It is an adhesive film composed of epoxy resin and a nylon scrim with the aim of preventing the reduction of epoxy resin in the CFRP.

- Application of CFRP plies onto the leveled surface, utilizing a Pre-Preg twill comprising GG-204T woven fabric impregnated with an epoxy matrix IMP503Z-HT. The chosen layup comprises eight plies with a regularly alternating orientation between 90 degrees and 45 degrees.
- Placement of a release film upon achieving the specified number of plies, followed by the addition of an aeration felt layer surrounding the mold and above the laminated components.
- Vacuum sealing of the jig using a vacuum bag before subjecting it to curing in an autoclave at 140 degrees Celsius and a pressure of 6 bar. The autoclave cycle employed is illustrated in Figure 1.
- Post-autoclave completion, manual cutting of the specimens is performed.
- Bonding of specific aluminum end-tabs at each end to mitigate bending during single lap tests, as depicted in Figure 1.
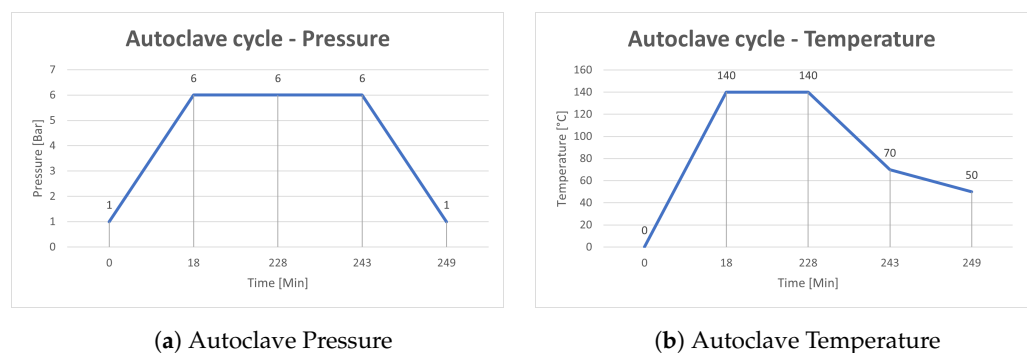

(**a**) Autoclave Pressure　　　　　　　　　　　(**b**) Autoclave Temperature

Figure 1. Autoclave's cycle.

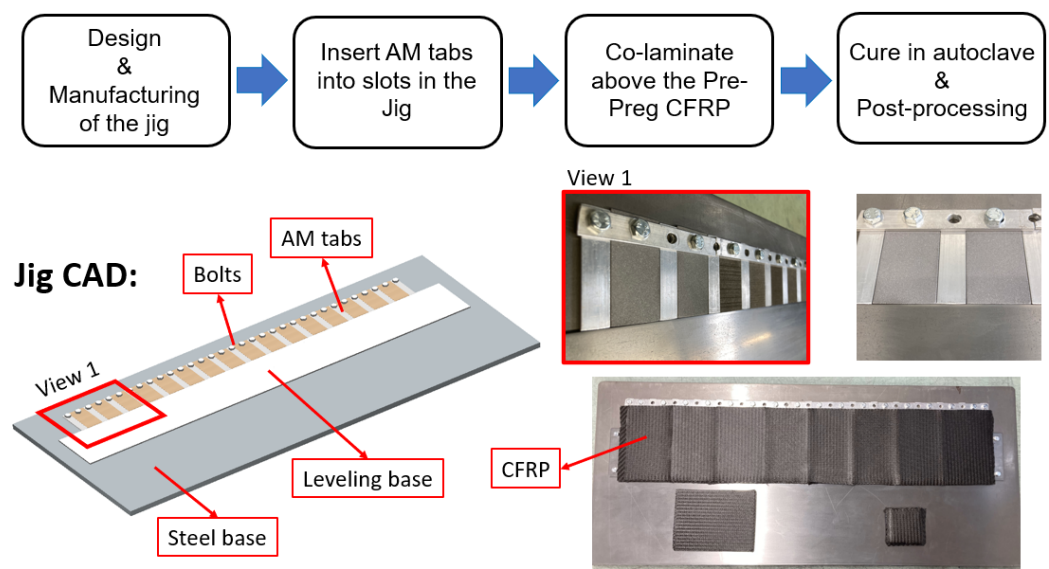This manufacturing process is elucidated in Figure 2.

Figure 2. Schematic illustration of the manufacturing process.

The metallic substrates are fabricated utilizing a LPBF Renishaw machine [29], employing a biomedical-grade Ti6Al4V alloy. The nominal power of the pulsed laser of the machine is 200 W with a layer thickness of 0.060 mm. The particle size of the material is in the range of 0.015 mm and 0.045 mm. Other specific details regarding printing parameters and powder specifications are withheld. As illustrated in Figure 3, the metal substrate comprises two distinct regions: a solid section featuring a hole intended for a potential bolted connection and a porous region designed for contact with the CFRP. The porous

section incorporates a Simple Cubic cell lattice structure, with variations in unit cell dimensions, including height h, width w, and the diameter of the struts d. Each specimen is uniquely coded for post-lamination identification. The as-designed dimensions of the metal substrate are presented in Table 1. Table 2 provides comprehensive characteristics of the seven distinct configuration of Hybrid Junction specimens. To ensure the robustness of the data, two specimens have been tested for each of the seven unique configurations of the Hybrid Junctions. Accordingly, a total of 14 specimens have been produced. Notably, specimens 1020 and 1520 are configured with pins positioned atop the lattice, situated at the vertices of the cubic cell. The pins share the same diameter d as the struts, and their height $hPins$ is documented in Table 2. Notice that in Table 2, the specimen 1005 has two different designations, named 1005_1 and 1005_2. This is due to the fact that this kind of specimen has two different dimensions of the SC cell on the lattice substrate.

Table 1. As-designed dimensions of the metal specimens.

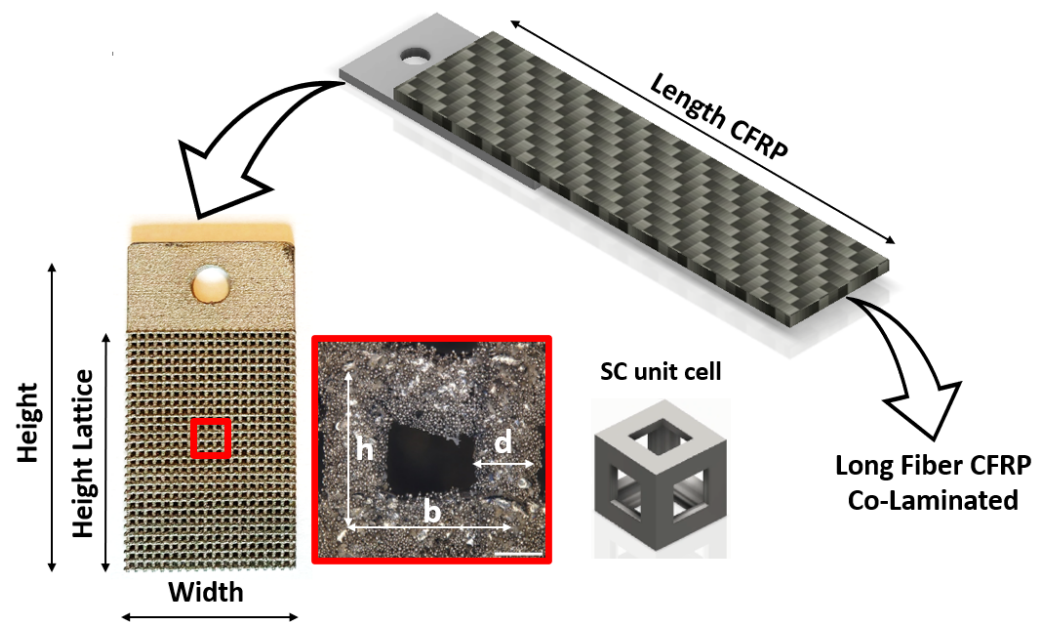| Width (mm)	Height (mm)	Height Lattice (mm)	Thickness (mm)
25	51	30	2.1

Figure 3. Design of the Single Lap Specimen with a focus on the 3D printed metal part. The microscope picture regards the Simple Cubic unit cell of the lattice substrate. Additionally, for enhanced clarity of the unit cell, a 3D representation is provided adjacent to the microscope image, labeled as the 'SC unit cell'.

Table 2. Theoretical dimensions of the SC unit cell.

Specimen Code	h [mm]	b [mm]	d [mm]	$hPins$ [mm]
1005_1	0.75	0.75	0.35	-
1005_2	1.45	0.75	0.35	-
1010	0.8	0.8	0.4	-
1020	0.9	0.9	0.55	0.25
1510	1.15	1.15	0.4	0.15
1520	1.25	1.25	0.55	-
0710	0.6	0.6	0.4	-
0720	0.7	0.7	0.55	-

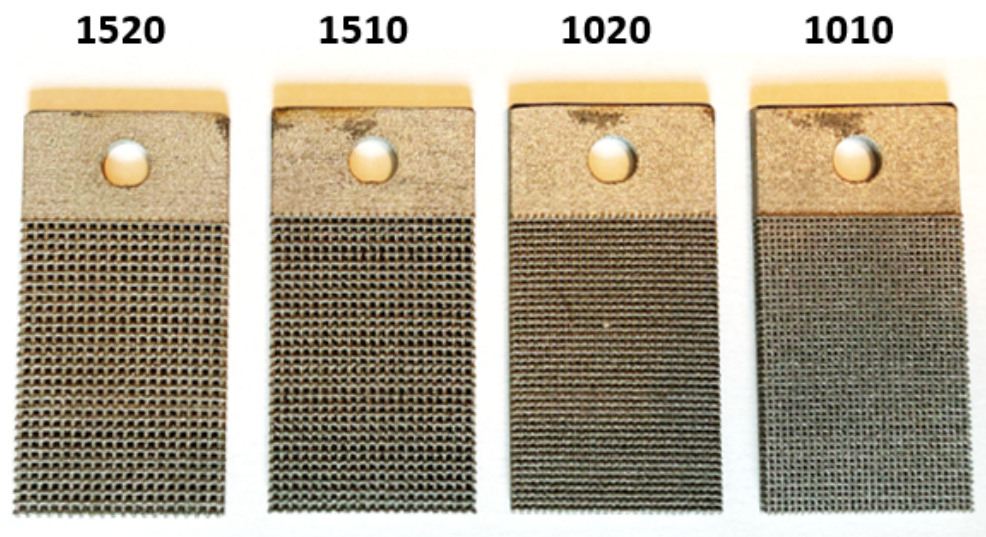Some of the listed metal specimens of Table 2, are shown in Figure 4

Figure 4. Different 3D printed metal specimens.

As part of the benchmark testing, we fabricated two "classical" junctions involving a bolted connection and a bonded connection. In these reference connections, the use of an AM titanium substrate was replaced by steel S235J2, specifically pickled and oiled. For the bolted connection, an M6 bolt of grade 8.8 was employed and tightened to a torque of 11 N m (Figure 5c). In the case of the bonded connection (Figure 5b), the steel substrate underwent superficial sandblasting with corundum grit 36, followed by an acetone cleaning, before being co-laminated using the procedure outlined earlier. To ensure repeatability, two specimens were produced for each type of junction. This comparative analysis allows for a comprehensive evaluation of the performance of the novel Hybrid Junctions against established benchmark connections, shedding light on the influence of substrate materials and connection methods on the overall mechanical behavior.

(**a**) Hybrid Junction   (**b**) Sandblasted steel junction   (**c**) Bolted junction

Figure 5. Three main different kinds of tested specimens.

2.2. Mechanical Testing

The specimens are subjected to single shear lap configuration testing following the guidelines outlined in ASTM D5868 [28]. A hydraulic machine, specifically the Instron 8516, equipped with a 100 kN load cell, is employed for this purpose. Hydraulic grips are utilized to clamp the specimens securely, mitigating the risk of potential slippage. The clamping pressure is set at 80 bar, a parameter tailored for aluminum materials. The testing velocity is fixed at 1 mm/min, and an extensometer is deployed to measure the elongation of the junction. Positioned on the CFRP side, the extensometer is situated 5 mm from the bottom edge of the metal part, as shown in Figure 6. Notably, the extensometer is removed after an observed elongation of 2 mm and prior to specimen failure.

For specimen alignment, as shown in Figure 6, specific aluminum end-tabs are affixed to the Single Lap specimens using commercial Loctite 9466 adhesive. These meticulous testing and alignment procedures are essential for obtaining accurate and reliable data on the mechanical behavior of the Hybrid Junctions under shear loading conditions.
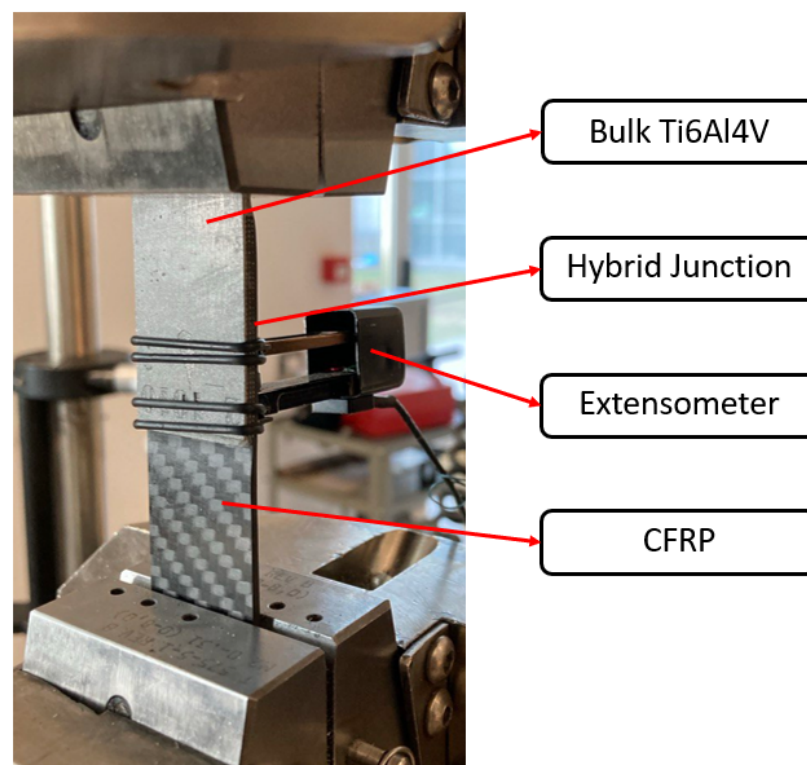

Figure 6. Test setup on the Instron 8516, as indicated for ASTM 5868.

2.3. FEM of the Junction

The FE model is performed usingANSYS APDL 2023 R1 (ANSYS, Pittsburgh, PA, USA). A schematic representation of the single lap test junction is depicted in Figure 7.
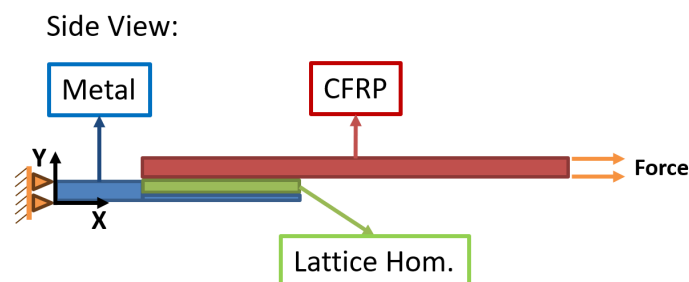

Figure 7. Simplification schema of the Hybrid Junction.

The model is composed by:

- A metal substrate, which includes also a layer at the bottom of the lattice structure;
- the lattice structure infilled by epoxy resin, which connects the metal part and the composite one;
- the composite part which lays above the lattice infilled material;

To replicate testing conditions, the metal substrate is anchored at one extremity, while the CFRP at the other extremity is subjected to a force consistent with experimental loads. To enhance the computational efficiency of the Finite Element Method (FEM), the intricate interaction among the lattice structure, resin, and CFRP is simulated using a simplified approach. Assuming a uniformly distributed resin in the lattice substrate as a reasonable hypothesis, the overall behavior is modeled by postulating the existence of a fictitious material amalgamating the properties of the two elements. These properties are computed using the Homogenization technique. Conversely, the CFRP component undergoes testing to derive its elastic properties. Given the straightforward geometry of the single lap specimen, the model is developed using 2D elements, further diminishing the computational cost of the simulation. This strategic modeling approach facilitates an efficient representation of the complex interplay within the Hybrid Junction while maintaining computational feasibility.

2.3.1. Homogenization Technique

To simulate the interaction between the resin and the lattice structure, a homogenized model has been developed [30,31]. The repetitive unit cell is substituted with an equivalent box possessing the corresponding material properties. A Representative Volume Element (RVE), comprising the Simple Cubic (SC) cell and its infilled volume with resin, has been formulated. Both sub-volumes are discretized using a solid quadratic mesh of Solid 186 elements. Special attention has been paid to mesh generation to attain symmetry and ensure the presence of symmetric nodes on opposite faces. This has enabled the implementation of periodic boundary conditions on the RVE. Nodes situated at the contact interface between the lattice structure and the epoxy resin infill are deliberately generated at coincident locations. By utilizing the merge command, a seamless simulation of perfect bonding between the two elements is achieved. This meticulous modeling approach aims to accurately capture the behavior of the Hybrid Junction, considering the complex interplay between the lattice structure and the resin during simulation. In Figure 8, are depicted the volumes for SC cell, epoxy resin, and the resulting RVE with the equivalent material properties.
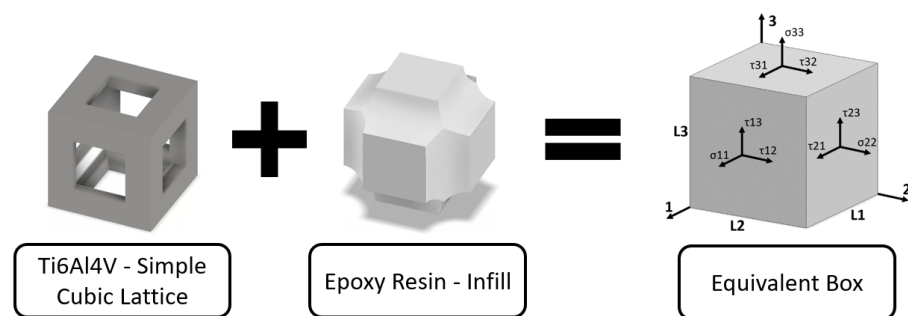
Figure 8. Homogenization process in which a complex and repeated structure is simplified with an equivalent box that has equivalent material properties.

Given the orthotropic nature of the material properties, it necessitates the execution of six distinct simulations to ascertain the elastic properties—three for compression and three for shear. The specific boundary conditions applied in each simulation are succinctly outlined in Table 3.

Table 3. Constraints used in the Homogenization process.

K Matrix Element	Side 1+	Side 1-	Side 2+	Side 2-	Side 3+	Side 3-	Load Type
K_{11}, K_{21}, K_{31}	$\delta_1 \neq 0$	$\delta_1 = 0$	$\delta_2 = 0$	$\delta_2 = 0$	$\delta_3 = 0$	$\delta_3 = 0$	Normal
K_{22}, K_{12}, K_{32}	$\delta_1 = 0$	$\delta_1 = 0$	$\delta_2 \neq 0$	$\delta_2 = 0$	$\delta_3 = 0$	$\delta_3 = 0$	Normal
K_{33}, K_{31}, K_{23}	$\delta_1 = 0$	$\delta_1 = 0$	$\delta_2 = 0$	$\delta_2 = 0$	$\delta_3 \neq 0$	$\delta_3 = 0$	Normal
K_{44}	$\delta_1 = 0$	$\delta_1 = 0$	$\delta_3 \neq 0$	$\delta_3 = 0$	$\delta_2 \neq 0$	$\delta_2 = 0$	Shear
K_{55}	$\delta_3 \neq 0$	$\delta_3 = 0$	$\delta_2 = 0$	$\delta_2 = 0$	$\delta_1 \neq 0$	$\delta_1 = 0$	Shear
K_{66}	$\delta_2 \neq 0$	$\delta_2 = 0$	$\delta_1 \neq 0$	$\delta_1 = 0$	$\delta_3 = 0$	$\delta_3 = 0$	Shear

As indicated in Table 2, samples 1020 and 1510 exhibit pins positioned above the lattice structure, precisely situated over the vertex of the Cubic unit cell, as illustrated in Figure 9. Following the co-lamination of CFRP above the metallic specimens, the pins are subsequently filled with epoxy resin. Consequently, the same homogenization technique employed previously for the SC unit cell has been utilized to simplify the representation of pins in the FE Model in this scenario as well. The resultant material properties have been incorporated into a slender layer situated between the CFRP and the Lattice homogenization. The model utilized is depicted in Figure 9.
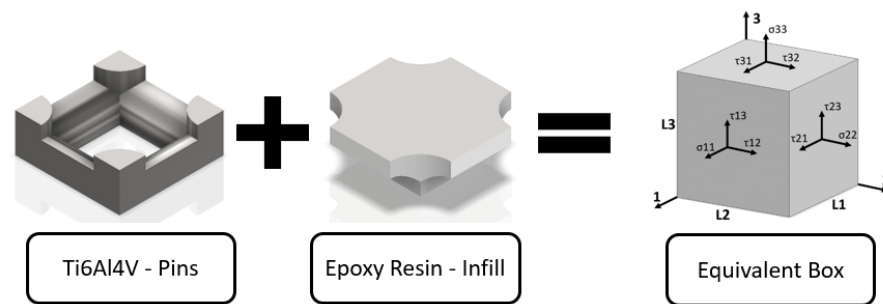

Figure 9. Homogenization process of pins that lay on the top surface of the 3D printed lattice specimens.

Table 4 presents the properties of the materials involved in the homogenization process. Titanium properties are sourced from the datasheet [29], while those of the Epoxy Resin are estimated from [32]. To assess the CFRP properties within the multilayered stack, a tensile test was conducted. The Young Modulus and the Poisson ratio were measured using a bi-axial extensometer on an Instron 5969 testing machine equipped with a 10 kN load cell. The tensile test, mirroring the CFRP layup used in the Hybrid Junction, employed two specimens of the same layup and overall length. Each specimen yielded two distinct sets of data: one for measurements along the axial direction and another for the transverse direction. Tests were confined to the linear region of the material, and the mean values derived from these tests are presented in Table 5. This comprehensive characterization of material properties is crucial for an accurate representation in the subsequent homogenized model.

Table 4. Properties of the material used.

Material Name	Young Modulus [GPa]	Poisson []
Ti6Al4V	126	0.34
Epoxy resin	3	0.33
CFRP	30.8 ± 1.7	0.367 ± 0.008
S235J2	200	0.33

Table 5. Properties of the material used.

Specimen Code	Axial Young Modulus [GPa]	Transverse Young Modulus [GPa]	Poisson []
CFRP$_1$	29.1	79.9	0.3585
CFRP$_2$	32.5	85.4	0.3751
ine Mean	30.8	82.7	0.3668

The outcomes of the homogenization process are succinctly summarized in Tables 6 and 7. Notably, in Table 6 the material properties derived exhibit isotropic characteristics owing to the cubic geometry of the cell. This observation underscores the influence of the structural arrangement on the overall mechanical behavior, emphasizing the isotropic nature of the homogenized material properties in the context of the cell's cubic geometry.

Table 6. Homogenized properties of the SC unit cell.

Specimen Code	Young Modulus [GPa]	Shear Modulus [GPa]	Poisson []
1005$_1$	29.18	5.14	0.192
1005$_2$ (y,z)	17.25	2.80	0.210
1005$_2$ (x)	26.56	3.35	0.227
1010	33.21	6.29	0.197
1020	48.65	11.83	0.223
1510	17.20	2.51	0.189
1520	25.89	4.33	0.191
0710	58.05	15.65	0.238
0720	79.43	25.54	0.278

Table 7. Homogenized properties of the Pins.

Specimen Code	E_{11} [GPa]	E_{22} [GPa]	E_{33} [GPa]	G_{23} [GPa]	G_{13} [GPa]	G_{12} [GPa]	ν_{23} []	ν_{13} []	ν_{12} []
1005$_1$	55.15	62.1	55.15	18.4	9.3	18.4	0.287	0.188	0.254
1005$_2$	51.7	49.5	32.2	10.5	4.3	16.7	0.294	0.187	0.282
1010	58.95	63.95	58.95	19.4	11.1	19.4	0.283	0.2	0.261
1020	42.4	46.9	42.4	9.8	10.4	9.8	0.222	0.226	0.2
1510	25.6	19.4	25.6	3.8	3.3	3.8	0.175	0.16	0.236
1520	51.8	55.5	51.8	16.3	7.98	16.3	0.273	0.179	0.255
0710	78.95	82.1	78.95	27.6	22.5	27.6	0.297	0.26	0.286
0720	92.9	92.5	92.9	33	31.2	33	0.304	0.295	0.305

2.3.2. Single Lap Shear Model

After completing the homogenization calculations for various structures and having established the CFRP properties through testing, the comprehensive simulation of the entire single lap specimen can be conducted. The model, depicted in Figure 7, has been discretized using a mapped mesh featuring quadratic Plane 183 2D elements, with the option of Plane Strain. This hypothesis is justified by the predominant width of the specimen in comparison to its thickness. To simulate a bonded contact between different materials, nodes have been merged. Figure 10 provides a detailed view of the mapped mesh utilized in the model. This modeling approach ensures a precise representation of the Hybrid Junction, allowing for a thorough examination of its mechanical behavior under specified loading conditions.

The model has been subjected to boundary conditions replicating the experimental test. The force is applied to the nodes situated on the surface of the grip area. These nodes undergo constraints, preventing all rotations and translations along the Y and Z axes. The only permitted movement is along the X axis, corresponding to the axis of the applied tensile force by the test bench.
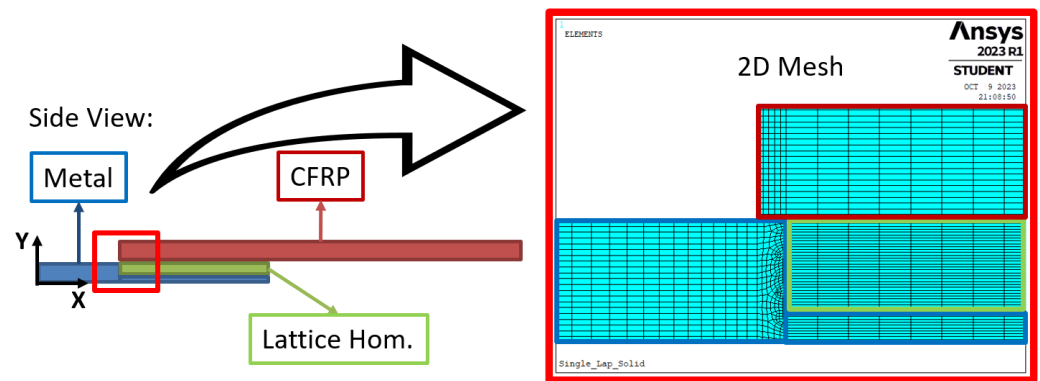
Figure 10. Details of the meshed junction.

Conversely, all nodes on the surface of the grip area of the composite part are constrained in all rotations and translations. This meticulous imposition of boundary conditions aligns the simulation with the real-world experimental setup, allowing for a meaningful and accurate representation of the response of Hybrid Junctions under specified loading conditions.

3. Results and Discussion

Novel Hybrid Junctions have been fabricated following the procedure outlined in Section 2.1. The resulting specimens are illustrated in Figure 11, with red boxes highlighting locations where there is minimal observable resin deficiency above the overlap area. However, measurements of CFRP thickness, taken both above the overlap area and at a considerable distance from it, reveal a notable difference. Specifically, the composite above the lattice exhibits reduced thickness due to a decrease in epoxy content.
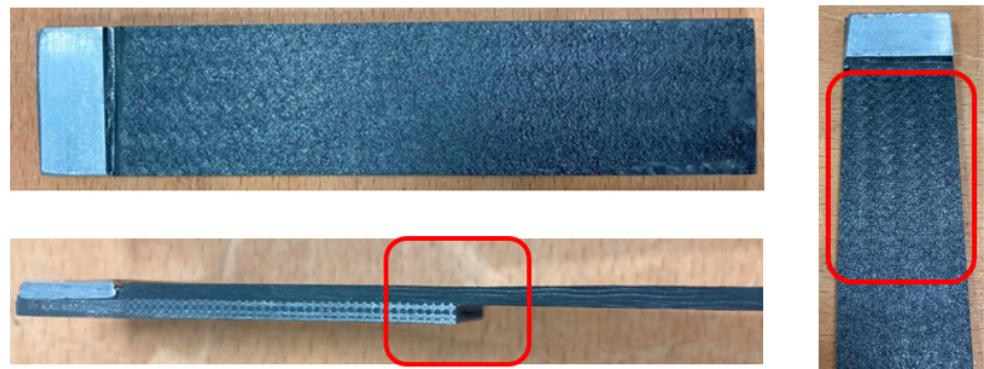

Figure 11. Observation of the produced Hybrid Junctions: within the red boxes we can appreciate the reduction of resin content above the overlap area.

The experimental outcomes of the tests, extending up to the removal of the extensometer, are depicted in Figure 12. Panel (a) represents Hybrid Junctions with SC cells, while panel (b) illustrates junctions with a sandblasted metal substrate. Subsequent to extensometer removal, the tests proceeded until the rupture of the specimens. A brittle failure was observed in all specimens. The ultimate load attained by each tested specimen, along with the Young Modulus of the junction, is detailed in Table 8. Two distinct average stresses of the junctions were computed: one for tensile stress (σ) and the second for shear stress (τ).
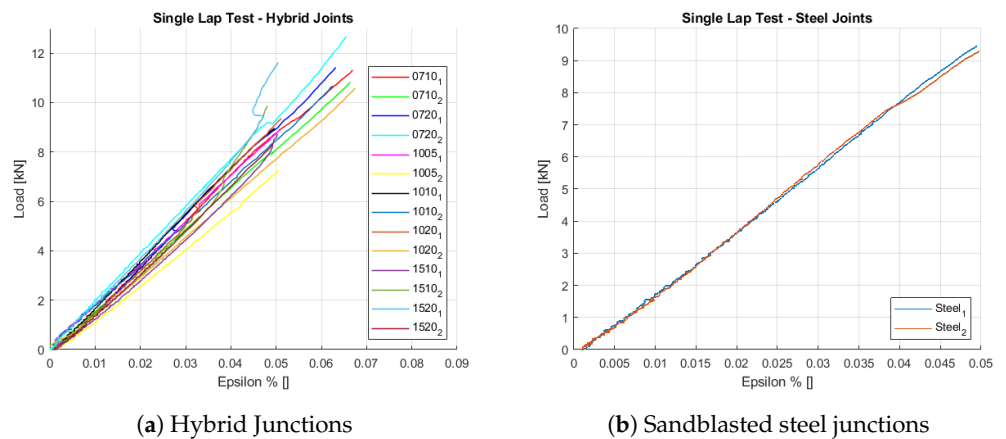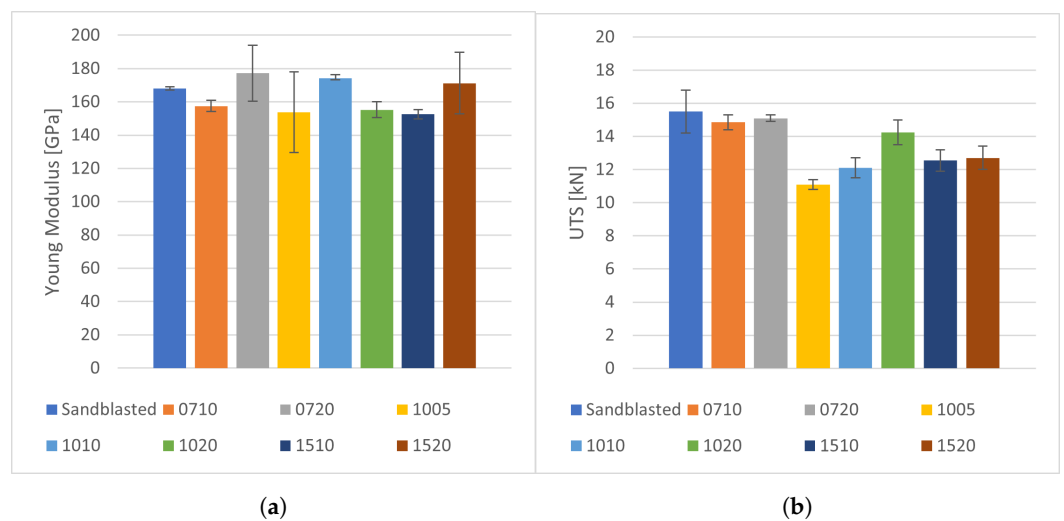
(**a**) Hybrid Junctions

(**b**) Sandblasted steel junctions

Figure 12. Results of the Single Lap tests performed.

Table 8. Results of the tested specimens.

Specimen Code	Young Modulus Junction [GPa]	Maximum Load [kN]	Average σ [MPa]	Average τ [MPa]
0710_1	160.8	14.4	142.8	16
0710_2	154.2	15.3	149.7	17
0720_1	160.4	14.9	150.5	16.6
0720_2	194.0	16.2	160.2	17.9
1005_1	178.0	11.4	116.6	12.7
1005_2	129.4	10.8	109.5	12
1010_1	172.0	12.7	126.3	14.1
1010_2	176.3	11.5	115.6	11.5
1020_1	160.1	13.5	138.9	15
1020_2	150.4	15	154.0	16.6
1510_1	149.8	13.2	142.5	14.7
1510_2	155.4	11.9	124.0	13.2
1520_1	189.7	13.4	137.3	14.8
1520_2	152.8	12.0	123.2	13.4
$Steel_1$	168.9	16.7	159.7	18.6
$Steel_2$	167.2	14.2	135.1	15.7

To enhance the representation of the results presented in Table 8, a visual comparison of the results has been conducted in Figure 13.

(**a**)

(**b**)

Figure 13. Comparison between sandblasted steel junctions and Hybrid Junctions: (**a**) Young Modulus. (**b**) Ultimate Tensile Stress.

Among the various Hybrid Junctions subjected to testing, specimen 0720_2 demonstrated the highest Young Modulus and Ultimate Load. Nevertheless, specimens featuring

a sandblasted steel substrate exhibited a superior Ultimate Load and enhanced repeatability in the Young Modulus compared to 0720_2.

A comparative analysis with a bolted junction has been conducted, and the results are depicted in Figure 14.
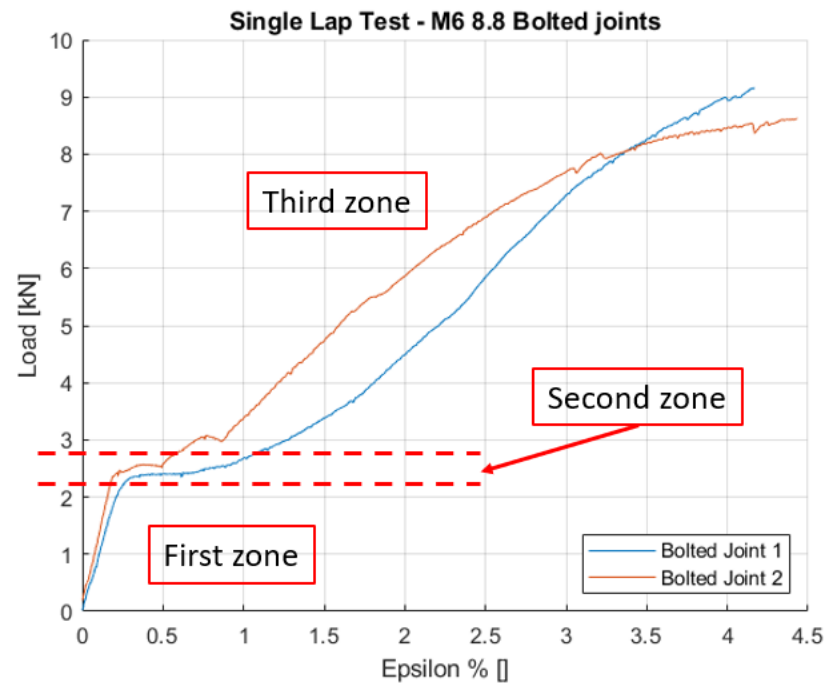

Figure 14. Raw Data of the Bolted junctions. Notice that there are three main zones. In the first zone the applied sliding load is transmitted by friction; the second zone is characterized by a plateau in which the two materials of the junction slide one against the other; in the third zone, the clearance between the bolt and the components has been recovered and thus, the bolt undergoes to pure shear up to failure.

The Load-Strain curve reveals three distinct regions: the initial region, characterized by the highest stiffness, where the applied sliding load is transmitted by friction; the second region featuring a plateau, indicating that the applied load surpasses the static friction load, leading to sliding between the two components; and the commencement of the third region, where the clearance between the bolt and the components has been recovered, resulting in the bolt functioning under pure shear load. The failure of the bolted junction occurred in the composite, adjacent to the hole, with the measured results outlined in Table 9. It is noteworthy that the maximum load achieved by the bolted junction is approximately half of the maximum load achieved by the co-laminated specimens. This observation underscores the contrasting mechanical behavior between the bolted junction and the co-laminated counterparts under the given loading conditions.

Table 9. Results of the Bolted junctions.

Specimen Code	Young Modulus [GPa]	First Peak [kN]	Maximum Load [kN]	Average Stress [MPa]
Bolted Joint$_1$	19.9	2.2	9.2	156
Bolted Joint$_2$	19.2	2.4	8.6	146.9
ine Mean	19.6 ± 0.3	2.3 ± 0.1	8.9 ± 0.3	151.5 ± 4.5

Figure 15 shows a comparison between the UTS achieved across the three principal categories of junctions. This visual representation aims to elucidate the disparities in UTS performance among these distinct junction types.
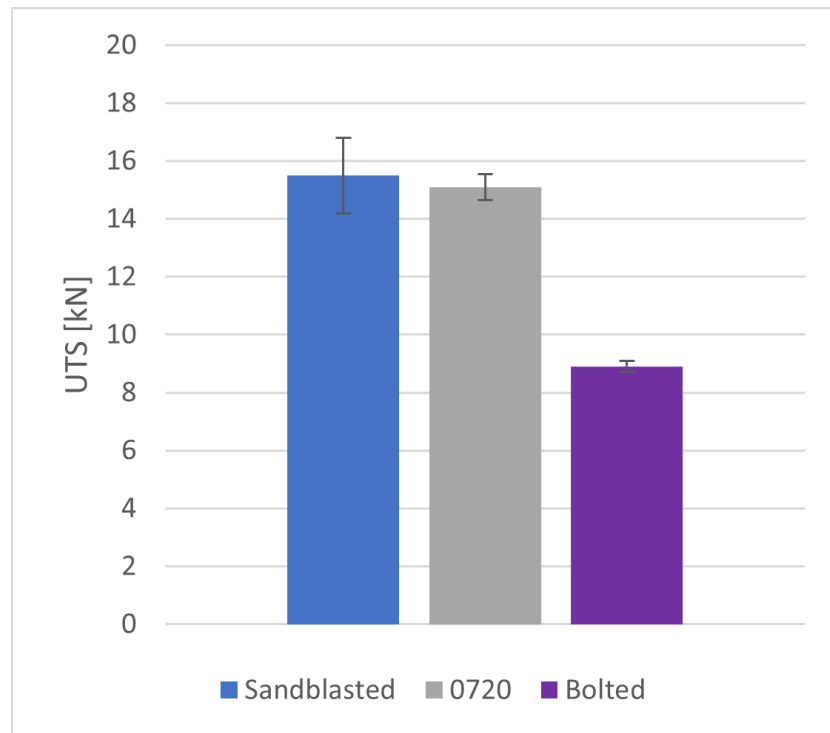
Figure 15. Comparison of the UTS between different junctions.

A comparative analysis between experimental results and Finite Element simulations is undertaken, and the outcomes for various junctions are detailed in Table 10. As outlined previously, the extensometer was positioned on the CFRP side over the overlap area, approximately 5 mm from the edge of the metal part, as illustrated in Figure 6. To maintain simulation fidelity to the actual tests, the deformation ($Deformation_{FEM}$) of the junction was measured between nodes located on the CFRP surface at the same distances as the real contact points of the extensometer. The disparity between displacements along the longitudinal axis of these two nodes was calculated to derive $Deformation_{FEM}$. To assess deformation within the linear region, a load equivalent to 4 kN was applied to the specimen along the longitudinal axis, and the Young Modulus was subsequently computed. This approach ensures a comprehensive comparison between experimental and simulated behaviors, contributing to a robust understanding of the mechanical response of junction.

Table 10. Comparison between real specimens and FEM simulation.

Specimen Code	$Deformation_{real}$ [mm]	E_{real} [GPa]	$Deformation_{FEM}$ [mm]	E_{FEM} [GPa]
1005	0.0190	155.0	0.0215	142.2
1010	0.0171	176.7	0.0218	137.1
1020	0.0192	162.1	0.0214	143.6
1510	0.0194	151.3	0.0235	134.9
1520	0.0170	171.4	0.0218	142.1
0710	0.0179	164.7	0.0197	150.5
0720	0.0161	177.4	0.0185	162.7

A graphical depiction of the outcomes presented in Table 10 is provided in Figure 16. The continuous red line represents the mean value, while the two dashed lines delineate the 95% confidence bounds. This visual representation offers a concise and informative overview of the data, enabling a clear understanding of the central tendency and the statistical variability in the results.
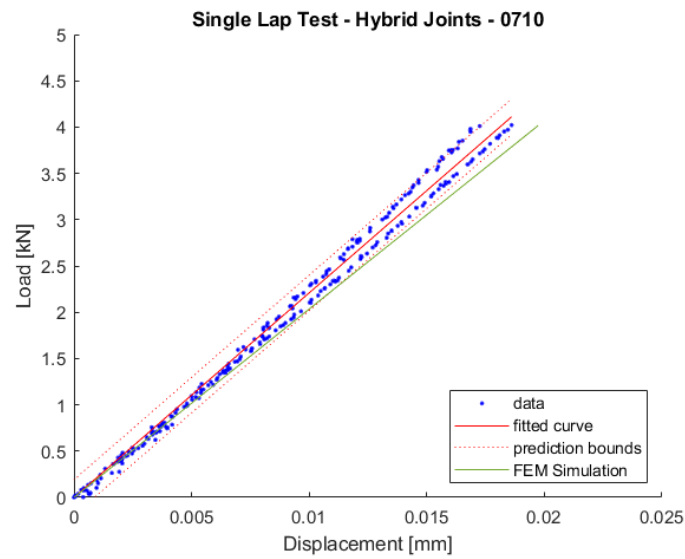
Figure 16. Specimen 0710: Comparison of the Young Modulus between real data and FEM simulation.

A discrepancy exists between the stiffness anticipated through Finite Element Method predictions and the actual measurements obtained in experimental trials. The FEM data consistently exhibit a lower slope compared to the real data, indicating a tendency to predict a more compliant junction. The percentage error between the two values falls within the range of 8.3% to 22.4%. The error, denoted as $\Delta Deformation$, represents the disparity between the measured deformation by the extensometer $Deformation_{real}$ and the simulated deformation $Deformation_{FEM}$.

$$\Delta Deformation = Deformation_{real} - Deformation_{FEM} \tag{1}$$

Also for the Young Modulus the error committed has been computed as:

$$\Delta E = E_{real} - E_{FEM} \tag{2}$$

The evaluation of errors are reported in Table 11.

Table 11. Difference between real specimen and theoretical model.

Specimen Code	ΔE [GPa]	$\Delta E_{percent}$ [%]	$\Delta Deformation$ [mm]
1005	12.8	8.3	0.0025
1010	39.6	22.4	0.0047
1020	18.5	11.4	0.0022
1510	16.4	10.8	0.0041
1520	29.3	17.1	0.0048
0710	14.2	8.6	0.0018
0720	14.7	8.3	0.0024

With the exception of specimens 1010 and 1520, discrepancies between the actual specimens and their simulated counterparts range from 8.3% to 11.4%. To mitigate these errors, an enhancement in the details level in the FE Model has been implemented. Specifically, a fillet with a radius R has been applied between the struts of the SC cell on two distinct specimens. The outcomes of these modifications are presented in Table 12.

Table 12. FEM simulation of the Single Lap junction considering fillets in the SC cell. Difference between real specimen and theoretical model.

Specimen Code	Radius R [mm]	$Deformation_{FEM}$ [mm]	E_{FEM} [GPa]
1510	0.25	0.0234	135.7
0720	0.08	0.0184	163.5

Comparing the results of Table 12 with the ones of Table 10, we can observe that the increase in stiffness is equal to 0.8 GPa for specimen 1510, which corresponds to an overall error between the real specimen and the simulated one equal to 10.3%. Whereas, for specimen 0720, we have an increase in stiffness in the FE Model equal to 0.8 GPa, which corresponds to a percentage error of 7.8%.

Microscopic Investigation

Following testing, specimens underwent cutting and polishing to examine the extent of resin infiltration within the lattice. A microscope investigation was conducted on three specific specimens: 1010, 1020, and 1520. Specimen 1010, chosen for its substantial volume of infilled resin, underwent optical microscope imaging, as depicted in Figure 17.

The images reveal uniform epoxy resin infiltration throughout the entire lattice structure, reaching the junction between the lattice and bulk material. Despite successful resin infiltration, visible pores are observed due to incomplete air removal from the vacuum.

Figure 17b displays that above the infilled lattice structure, a portion of the co-laminated CFRP remains. Examination of the analyzed specimen indicates failure occurred between the first and second layers of CFRP. The longitudinal fibers of the first layer remain bonded to the metal substrate, while the normal fibers are detached from the layers below.

A potential cause of CFRP failure is attributed to its low Inter-laminar Shear Strength (ILSS), heavily dependent on epoxy resin properties and quantity. Consequently, the reduction in resin quantity resulting from epoxy infiltration in the lattice (as shown in Figure 11) may have diminished the ILSS of the composite. To address this, it is proposed to reduce the volume available for resin flow, ensuring the correct epoxy quantity in the composite. Potential solutions include decreasing the height of the lattice substrate or reducing the dimensions of the unit cell.
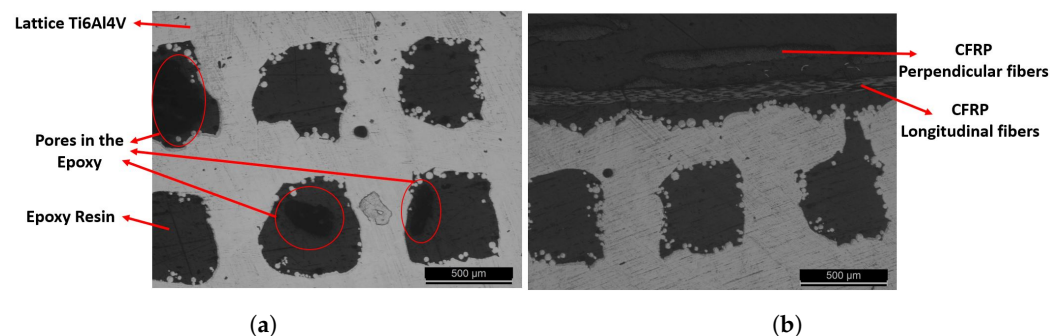

(**a**)   (**b**)

Figure 17. Microscope pictures of the impregnated Simple Cubic lattice structure—Specimen 1010. (**a**) shows a cross section of the impregnated lattice. Some pores in the Epoxy infill have been found. Additionally, (**b**) shows the upper part of a cross section of the junction, in which it is shown that the failure of the junction happened in between the first and second layers of the CFRP layup.

The detailed analysis of specimen 1020 sheds light on the impact of pins on the top surface of the lattice structure. Figure 18a depicts the cross-section between pins, while Figure 18b,c showcase the cross-section in the middle of a row of pins. A comparison between the two images reveals that the distance between the first layer of CFRP and the top surface is influenced by the presence of pins. Notably, the pins do not penetrate the first layer of CFRP, and the fibers of the ply do not conform to the shape of the pin. Consequently, the CFRP remains flat above the pins, resulting in no direct mechanical interaction between the pins and carbon fiber. In this specimen, failure occurred at the junction between the lattice structure and the CFRP. One possible explanation is that the pins acted as superficial imperfections, intensifying stresses in the area between the two materials and potentially creating a point of failure in the junction.
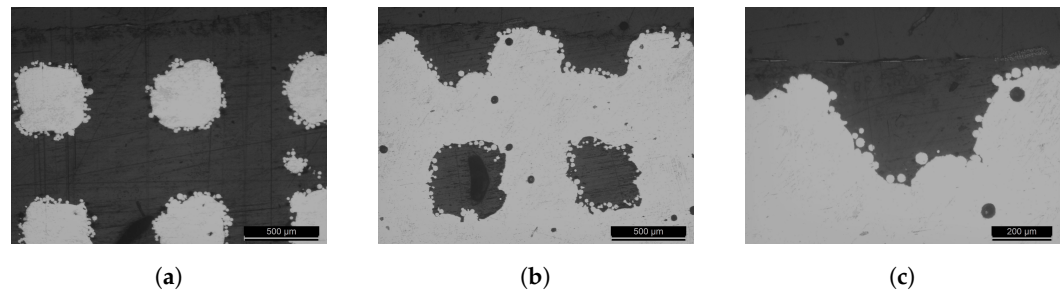
(**a**)   (**b**)   (**c**)

Figure 18. Microscope pictures of the impregnated Simple Cubic lattice structure—Specimen 1020. In (**a**,**b**) there is shown two different cross section of the impregnated lattice. Instead, in (**c**), there is a zoom on the impregnated pin of the junction.

Specimen 1520 experienced failure within the layers of CFRP, necessitating a thorough analysis. In Figure 19a, representing specimen 1520, the first layer of CFRP remains attached to the lattice structure. Notable failures are evident in Figure 19b,c. The first failure image reveals an inter-laminar failure, propagating through the fibers of the first layer and extending down to the layer of epoxy resin situated between the carbon fiber and the lattice structure. In contrast, the second image depicts broken fibers and a failure that propagated just beneath them. Figure 19b in the middle highlights the presence of pores within the resin volume. The description regarding pores and resin content aligns with that of specimen 1010.
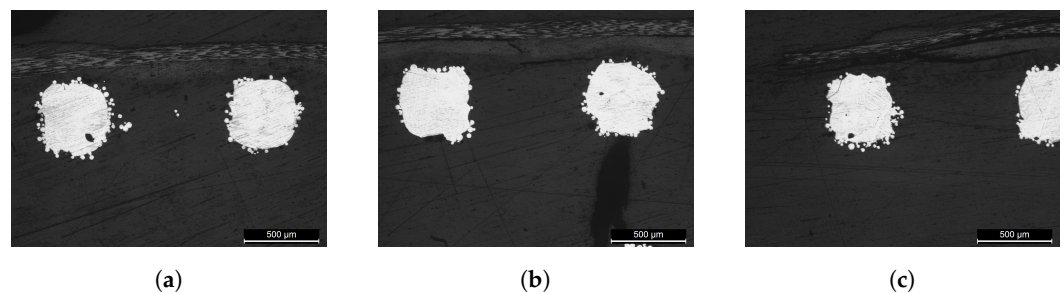

(**a**)   (**b**)   (**c**)

Figure 19. Microscope pictures of the impregnated Simple Cubic lattice structure—Specimen 1520. (**a**–**c**) show three different cross sections of the impregnated lattice. Notice the failure propagation in between the first layer of CFRP and the lattice.

4. Conclusions

Single lap Hybrid Junctions consist of two distinct materials: Pre-Preg Carbon Fiber Reinforced Polymer co-laminated onto a 3D printed Ti6Al4V metal specimen. To enhance adhesion, a lattice substrate with a Simple Cubic unit cell has been employed on the metal part, featuring seven variants with different SC cell dimensions. A comparative analysis was conducted between the novel junctions and two standard junctions:

- Bolted Junction: CFRP is laminated separately, and after curing the epoxy resin, the two materials are joined with an M6 bolt (grade 8.8) tightened at 11 N m;
- Sandblasted Junction: The steel specimen undergoes sandblasting with corundum grit 36, followed by co-lamination of CFRP.

Single lap tests were conducted following ASTM D5868, yielding the following results:

- Bolted junction: Withstands up to 2 kN, experiencing failure at around 8 kN next to the hole in the CFRP;
- Best co-laminated 3D printed Hybrid Junction (0720): Withstands loads up to 15 kN in the linear region, exhibiting a Young Modulus between 160 GPa and 194 GPa. It reaches a peak shear stress of 17.9 MPa with a mean value of 17.3 MPa;
- Sandblasted steel junction: Achieves a mean Young Modulus of 168 GPa and a maximum load ranging between 14.2 kN and 16.7 kN.

The new 3D printed titanium Hybrid Junction demonstrates comparable results to the sandblasted steel counterpart. Despite the lower adhesion of epoxy resin on titanium compared to Steel, the achieved results are promising.

An FE Method was employed to model various Hybrid Junctions using 2D plane elements. To enhance computational efficiency, the infilled lattice structure was simplified using the Homogenization technique. Despite simplifying assumptions, the FEM accurately predicted the behavior of real specimens with a good level of accuracy, except for specimens 1010 and 1520, where errors ranged between 8.3% and 11.4%. Experimental data consistently demonstrated slightly greater stiffness than FEM simulations. Assumptions included untestable properties of the epoxy resin, altered during Pre-Preg composite manufacturing. Autoclave curing removed volatile particles, affecting a hypothetical pure epoxy specimen. Discrepancies also arose from different dimensions of cells and struts in the FE Model compared to theoretical values, assuming perfect material adhesion. Incorporating fillets in lattice structures reduced errors in FEM predictions, as observed in Table 12. Measurement-related issues arose from placing the extensometer on the CFRP side, causing compression due to the bending of the single lap junction. This compression led to reduced displacement measurements compared to FEM simulations, primarily measuring pure X-axis deformation. Regarding resin infiltration in different Simple Cubic cell sizes, epoxy uniformly filled the lattice substrate, with visible pores containing trapped air. Microscope investigation of specimens 1010 and 1520 (Figure 17 and Figure 19, respectively) revealed junction failures between the first and second layers of the CFRP layup. While the Ti6Al4V-CFRP interface remained bonded, the weakest link was attributed to the CFRP layup's low Inter-laminar Shear Strength. The reduced epoxy resin content in the stack could enhance the junction's mechanical properties by minimizing lattice substrate thickness. As shown in Figure 18, specimens with pins on the top surface exhibited detachment of CFRP from the top surface, indicating the weakest point was the interface between the two materials. Additionally, the pins did not penetrate the carbon fiber plies, demonstrating a lack of mechanical interaction between the metal and fibers. Limitations of the project arise primarily from the decision to exclusively test titanium with a singular set of printing parameters, potentially leading to fluctuations in the obtained test results. Moreover, the investigation was restricted to the SC cell within a specified dimensional range, indicating the potential for broader exploration across a wider spectrum of dimensions and the inclusion of other cell types for a more comprehensive analysis. Additionally, the project's scope was further constrained by the use of only one type of CFRP ply. This limitation underscores the necessity to explore various fabric types of CFRP and, importantly, different epoxy resins.

Author Contributions: Conceptualization, A.C., R.D.B., F.S. and M.B.; Investigation, A.C., D.R. and F.S.; Methodology, A.C. and R.D.B.; Supervision, A.P. and M.B.; Writing—original draft, A.C. and R.D.B.; Writing—review & editing, D.R., F.S., A.P. and M.B. All authors have read and agreed to the published version of the manuscript.

Data Availability Statement: The data presented in this study are available on request from the corresponding author.

Conflicts of Interest: Author Fabrizio Stecca was employed by the company Novation Tech S.P.A. The remaining authors declare that the research was conducted in the absence of any commercial or financial relationships that could be construed as a potential conflict of interest

Abbreviations

The following abbreviations are used in this manuscript:

CFRP	Carbon Fiber Reinforced Polymer
FEM	Finite Element Model
SC	Simple Cubic
SLS	Selective Laser Sintering
Pre-Preg	Pre-Impregnated
E	Young Modulus
UTS	Ultimate Tensile Strength
σ	Stress
τ	Shear Stress
ϵ	Strain
γ	Shear Strain
δ	Deformation

References

1. Zhu, J.H.; Zhang, W.H.; Xia, L. Topology Optimization in Aircraft and Aerospace Structures Design. *Arch. Comput. Methods Eng.* **2016**, *23*, 595–622. https://doi.org/10.1007/s11831-015-9151-2.

2. Shercliff, H.; Ashby, M. *Elastic Structures in Design*; Elsevier: Amsterdam, The Netherlands, 2016. https://doi.org/10.1016/B978-0-12-803581-8.02944-1.

3. Galińska, A.; Galiński, C. Mechanical Joining of Fibre Reinforced Polymer Composites to Metals—A Review. Part II: Riveting, Clinching, Non-Adhesive Form-Locked Joints, Pin and Loop Joining. *Polymers* **2020**, *12*, 19–23. https://doi.org/10.3390/polym12081681.

4. Kirsch, E.G. Die Theorie der Elastizität und die Bedürfnisse der Festigkeitslehre. *Z. Vereines Dtsch. Ingenieure* **1898**, *42*, 797–807.

5. Qin, G.; Na, J.; Mu, W.; Tan, W. Effect of thermal cycling on the degradation of adhesively bonded CFRP/aluminum alloy joints for automobiles. *Int. J. Adhes. Adhes.* **2019**, *95*, 102439. https://doi.org/10.1016/j.ijadhadh.2019.102439.

6. Viana, G.; Costa, M.R.N.; Banea, M.D.; da Silva, L.F.M. A review on the temperature and moisture degradation of adhesive joints. *Proc. Inst. Mech. Eng. Part L J. Mater. Des. Appl.* **2017**, *231*, 488–501.

7. Hwang, J.; Jin, C.; Min Sik, L.; Choi, S.; Kang, C. Effect of Surface Roughness on the Bonding Strength and Spring-Back of a CFRP/CR980 Hybrid Composite. *Metals* **2018**, *8*, 716. https://doi.org/10.3390/met8090716.

8. Li, C.; Viswanathan-Chettiar, S.; Sun, F.; Shi, Z.; Blackman, B. Effect of CFRP surface topography on the adhesion and strength of composite-composite and composite-metal joints. *Compos. Part A Appl. Sci. Manuf.* **2023**, *164*, 107275. https://doi.org/10.1016/j.compositesa.2022.107275.

9. Kim, K.; Jung, Y.; Yang, B.J.; Kim, J. Adhesion enhancement and damage protection for carbon fiber-reinforced polymer (CFRP) composites via silica particle coating. *Compos. Part A Appl. Sci. Manuf.* **2018**, *109*,105–114. https://doi.org/10.1016/j.compositesa.2018.02.042.

10. Hu, Y.; Liu, X.; Ji, F.; Wei, J.; Jiang, W.; Zhang, Y. Effects of the Electrophoretic Deposition of CNTs on the Mechanical Properties of Ti/CFRP Composite Laminates. *ACS Omega* **2022**, *7*, 1337–1346. https://doi.org/doi:10.1021/acsomega.1c05956.

11. Zuo, S.; Wang, L.; Zhang, J.; Yang, G.; Xu, Y.; Hu, Y.; Cheng, F.; Hu, X. Comparative Study of Resin and Silane Coupling Agents Coating Treatments on Bonding Strength Improvement of Titanium and Carbon Fiber Composites. *Coatings* **2023**, *13*, 903. https://doi.org/10.3390/coatings13050903.

12. Gardiner, G. Hyperjoint: Additive Metal + Composites = Stronger, Tougher Joints 2020. Available online: https://www.compositesworld.com/articles/hyperjoint-additive-metal-composites-stronger-tougher-joints#:~:text=Hyperjoint%20is%20a%20patented%20technology,of%20additive%20manufacturing%20metal%20components (accessed on 15 November 2023).

13. Parkes, P.; Butler, R.; Meyer, J.; de Oliveira, A. Static strength of metal-composite joints with penetrative reinforcement. *Compos. Struct.* **2014**, *118*, 250–256. https://doi.org/10.1016/j.compstruct.2014.07.019.

14. La Rocca, G. Progettazione di Giunzioni Ibride Ti6Al4V-CFRP. Master's Thesis, Politecnico di Torino, Turin, Italy, 2020. Available online: http://webthesis.biblio.polito.it/id/eprint/19468 (accessed on 18 October 2023).

15. Ferrari, M. Structurally Optimized and Additively Manufactured Inserts for Sandwich Panels of Spacecraft Structures. Master's Thesis, University of ETH-Zurich, Zurich, Switzerland, 2015.

16. Qi, G.; Chen, Y.L.; Rauschen, P.; Schröder, K.U.; Ma, L. Characteristics of an improved boundary insert for sandwich panels with lattice truss cores. *Aerosp. Sci. Technol.* **2020**, *107*, 2–12. https://doi.org/10.1016/j.ast.2020.106278.

17. DebRoy, T.; Wei, H.; Zuback, J.; Mukherjee, T.; Elmer, J.; Milewski, J.; Beese, A.; Wilson-Heid, A.; De, A.; Zhang, W. Additive manufacturing of metallic components—Process, structure and properties. *Prog. Mater. Sci.* **2018**, *92*, 112–224. https://doi.org/10.1016/j.pmatsci.2017.10.001.

18. Fleck N. A., D.V.S.; F., A.M. Micro-architectured materials: Past, present and future. *Proc. R. Soc.* **2010**, *466*, 2495–2516. https://doi.org/http://doi.org/10.1098/rspa.2010.0215.

19. Helou, M.; Kara, S. Design, analysis and manufacturing of lattice structures: An overview. *Int. J. Comput. Integr. Manuf.* **2018**, *31*, 243–261. https://doi.org/10.1080/0951192X.2017.1407456.

20. Wendy Gu, X.; Greer, J.R. Ultra-strong architected Cu meso-lattices. *Extrem. Mech. Lett.* **2015**, *2*, 7–14. https://doi.org/10.1016/j.eml.2015.01.006.

21. Messner, M.C. Optimal lattice-structured materials. *J. Mech. Phys. Solids* **2016**, *96*, 162–183. https://doi.org/10.1016/j.jmps.2016.07.010.

22. Tancogne-Dejean, T.; Spierings, A.B.; Mohr, D. Additively-manufactured metallic micro-lattice materials for high specific energy absorption under static and dynamic loading. *Acta Mater.* **2016**, *116*, 14–28. https://doi.org/10.1016/j.actamat.2016.05.054.

23. Van Tonder, T.; Langdon, G.S.; Von Klemperer, C.J. Adhesive Properties of Thermoset Fibre Metal Laminates. Master's Thesis, University of Cape Town, Cape Town, South Africa, 2014.

24. Sadighi, M.; Alderliesten, R.; Benedictus, R. Impact resistance of fiber-metal laminates: A review. *Int. J. Impact Eng.* **2012**, *49*, 77–90. https://doi.org/10.1016/j.ijimpeng.2012.05.006.

25. Li, X.; Tan, Y.H.; Wang, P.; Su, X.; Willy, H.J.; Herng, T.S.; Ding, J. Metallic microlattice and epoxy interpenetrating phase composites: Experimental and simulation studies on superior mechanical properties and their mechanisms. *Compos. Part A Appl. Sci. Manuf.* **2020**, *135*, 105934. https://doi.org/10.1016/j.compositesa.2020.105934.

26. Mines, R.; Tsopanos, S.; Shen, Y.; Hasan, R.; McKown, S. Drop weight impact behaviour of sandwich panels with metallic micro lattice cores. *Int. J. Impact Eng.* **2013**, *60*, 120–132. https://doi.org/10.1016/j.ijimpeng.2013.04.007.

27. S. J. Hollister, N.K. A comparison of homogenization and standard mechanics analyses for periodic porous composites. *Comput. Mech.* **1992**, *10*, 73–95.

28. *ASTM D5868*; Standard Test Method for Lap Shear Adhesion for Fiber Reinforced Plastic (FRP) Bonding. ASTM International: West Conshohocken, PA, USA, 2014. Available online: https://www.astm.org/d5868-01r14.html (accessed on 5 December 2023).

29. Renishaw. Schede Tecniche—PRODUZIONE Additiva. Available online: https://www.renishaw.it/it/schede-tecniche-produzione-additiva--17862 (accessed on 5 December 2023).

30. M. Dallago, M. Benedetti, V.L.; Fontanari, V. Orthotropic elastic constants of 2D cellular structures with variously arranged square cells: The effect of filleted wall junctions. *Int. J. Mech. Sci.* **2017**, *122*, 63–67.

31. Robert Millard Jones, K.S.D. *Mechanics of Composite Materials*; Springer: Berlin/Heidelberg, Germany, 1999; Volume 2, pp. 55–73.

32. Salim Yamini, R.J.Y. The mechanical properties of epoxy resins. *J. Mater. Sci.* **1980**, *15*, 1814–1822. https://doi.org/10.1007/BF00550602.